Hexagonal-BN filler boosts electrochemical performance of polymeric solid-state electrolyte for sodium-metal batteries

Shuangwu Xu[a,†], Le Zhao[a,†], Zheting Liu[a], Huapeng Sun[b], Dan Sun[a], Zhiguang Peng[a*], Yougen Tang[a], Wenyao Wang[c] and Haiyan Wang[a, c*]

[a] Hunan Provincial Key Laboratory of Chemical Power Sources, College of Chemistry and Chemical Engineering, Central South University, Changsha 410083, China

[b] School of New Energy, Chenzhou Vocational Technical College; Chenjiang Laboratory, Chenzhou 423000, China

[c] Hunan Yihua New Energy Co., Ltd

[*] Corresponding author

E-mail addresses: wanghy419@csu.edu.cn (Haiyan Wang); zhigpeng@csu.edu.cn (Zhiguang Peng)

[†] These authors contributed equally to this work

1. Experimental Section

1.1. Synthesis of Solid-State Electrolytes

h-BN particles were purchased from Aladdin and held at 120°C for 12 h to fully dry before use. Sodium bis(trifluoromethylsulfonyl)imide (NaTFSI) was purchased from Dodo Chemical Technology Ltd. We prepared CPE membranes using the film-casting method. Typically, PVDF-HFP (Mw = 400,000, Sigma-Aldrich) and NaTFSI (1:0.8 weight ratio) were first dissolved in a mixed solvent (1:3 of N,N-dimethylformamide (DMF, 99.8%, Aladdin) and acetone (AR, ChengDu Chron Chemicals Co., Ltd.)). After proper stirring, an appropriate amount of h-BN (mass ratio of h-BN: PVDF-HFP = 0, 0.1, 0.2, 0.3) was added. After sufficient stirring for 6 h, 0.2 mL of fluoroethylene carbonate (FEC, Dodo Chemical Technology Ltd.) was added to the solution and stirred for 1 h again. Then, the electrolyte slurry was cast onto a glass plate using a spatula with a thickness of 1000 μm. Finally, the film was further dried under vacuum at 60°C for 12 h to obtain the film and stored in an argon-filled glove box for use. The obtained CPEs were noted as PVDF-HFP/NaTFSI SPE, PVDF-HFP/NaTFSI/10BN CPE, PVDF-HFP/NaTFSI/20BN CPE, and PVDF-HFP/NaTFSI/30BN CPE, respectively.

1.2. Material Characterization

The crystal structures of both h-BN and SSEs were confirmed by powder X-ray diffraction (XRD, SmartLab 3kW, Rigaku Corporation) using Cu-Kα radiation. The microscopic morphology of the materials was observed using field emission scanning electron microscopy (FE-SEM, TESCAN MIRA3), while the elemental distribution of the samples was determined using energy dispersive spectroscopy (EDS, Bruker Quantax). Fourier transform infrared spectroscopy (FTIR) spectral measurements were conducted on a Thermo Scientific Nicolet iS50. Thermogravimetric

analysis (TGA) using a Netzsch STA 449F3 instrument with a rate of 10 °C·min^{-1} from 25 to 600 °C under a nitrogen (N_2) atmosphere to evaluate the thermal stability of CPEs. Raman spectra were collected on a RENISHAW inVia Reflex Raman microscope (UK). X-ray photoelectron spectroscopy (XPS) was measured by an X-ray photoelectron spectroscopy (NEXSA, Thermo Fisher Scientific). The tensile strength was measured by a tensile machine (Universal Testing Machine, WDW-6100, Jinan Fengzhi Test Instrument Co., Ltd., China) with a stretching rate of 10 mm/min. The data collection of the pouch cell is measured by the Feli-1200 ultrasonic battery scanning system.

1.3. Electrochemical Measurements

All CR2016-type coin cell cells were assembled in a glove box (H_2O < 0.1 ppm, O_2 < 0.1 ppm) for the electrochemical tests. The electrochemical stability window (ESW) was estimated by linear scanning voltammetry (LSV) on an electrochemical workstation (Multi Autolab M204) using stainless steel as the working electrode and sodium metal as the counter and reference electrodes over the voltage range of 0 to 6 V at a scan rate of 0.2 mV·s^{-1}. The cyclic voltammetry (CV) measurements were measured by a Multi Autolab M204 in NVP || PVDF-HFP/NaTFSI/BN CPEs || Na cells at a scanning rate of 0.1 mV·s^{-1}. The ionic conductivity σ (S·cm^{-1}) of the electrolyte membrane was calculated by measuring the electrochemical impedance spectra (EIS) of a stainless steel || SSE || stainless steel CR2016-type coin symmetric cell at a frequency of 10^6 to 10 Hz. The ionic conductivity was calculated according to the following equation (1):

$$\sigma = \frac{l}{R \times S} \tag{1}$$

where l (cm) is the thickness of the electrolyte (d = 0.0065 cm), S (cm^2) is the effective contact area with the stainless steel (Φ = 16 mm), and R (Ω) is the resistance measured by EIS. The E_a was

calculated according to the following Arrhenius equation (2):

$$\sigma = Aexp\left(-\frac{E_a}{RT}\right) \quad (2)$$

where A is the pre-exponential factor, R is the thermodynamic constant, and T is the absolute temperature.

The Na^+ transference number (t_{Na^+}) was obtained by combined DC polarization/AC impedance using a Na || SSE || Na 2016-type coin symmetric cell. The t_{Na^+} was obtained by calculating the following equation (3):

$$t_{Na^+} = \frac{I_S(\Delta V - I_0R_0)}{I_0(\Delta V - I_SR_S)} \quad (3)$$

where I_0 and I_s are the initial and steady-state current values, and R_0 and R_s are the interfacial resistances before and after polarization. ΔV is the polarization potential with 10 mV used in this work.

The $Na_3V_2(PO_4)_3$ (NVP) cathode was acquired by coating the mixed slurry of commercial NVP, polyvinylidene fluoride (PVDF) binder, and super P conductor with a mass ratio of 8:1:1 on carbon-coated aluminum foil and dried at 80 °C under vacuum for 12 h. The average mass loading of NVP active material was 1.5~2.0 $mg \cdot cm^{-2}$. The batteries were activated at 0.1 C (1 C = 110 $mA \cdot g^{-1}$) for 3 cycles before testing. The charge-discharge tests of cells were conducted on the CT-4008T Neware battery testing system at 30 °C between 2.0 and 3.8 V. To evaluate the practical performance of CPE, the NVP cathode and sodium tablet (5.5 cm × 6 cm) were stacked and placed in a laminate pouch bag. After vacuum sealing, solid-state pouch cells were obtained.

1.4. Density Functional Theory (DFT) Calculation

To probe the interactions between h-BN and $TFSI^-$ in CPEs, the adsorption energies were investigated based on DFT calculations performed by the DMol^3 code. The generalized gradient

approximation with the Perdew–Burke–Ernzerhof (PBE) functional and double numerical plus polarization (DNP) basis was used to describe the exchange-correlation potential. The optimal geometric convergence criteria of energy iteration, force, and atomic displacement were 1.0×10^{-5} Ha, 2×10^{-3} Ha Å, and 5×10^{-3} Å, respectively. The Monkhorst–Pack scheme with $2 \times 2 \times 1$ k-point was used for structural optimization. To reduce the interactions between neighboring layers, the vacuum thickness was set to be more than 15 Å. The formula for adsorption energy is defined as follows.

$$E_b = E_{total} - E_{TFSI^-} - E_{h-BN} \quad (4)$$

where E_{total}, E_{TFSI^-}, and $E_{h\text{-}BN}$ denote the energies of h-BN–TFSI$^-$, TFSI$^-$, and pristine h-BN (0 0 2), respectively.

Table S1. Molecular vibration results in the PVDF-HFP/NaTFSI/20BN CPE.

DMF (cm^{-1})	PVDF-HFP (cm^{-1})	$TFSI^-$ (cm^{-1})	Description of bands
		614	out-of-phase asymmetric bending SO_2
		651	bending SNS
		741	symmetric bending CF_3
		768	symmetric stretching SNS
		791	symmetric stretching CS
	837		α-phase band
	878		amorphous band
		1056	asymmetric stretching SNS
		1135	symmetric stretching SO_2
		1173	asymmetric stretching CF_3
		1331	out-of-phase asymmetric stretching SO_2
		1349	in-phase asymmetric stretching SO_2
	1391		asymmetric stretching CF_2
1659			stretching C=O

Table S2. Comparative analysis of electrochemical performance

Materials	Q_R ($mAh \cdot g^{-1}$)	Capacity Retention	Rate performances ($mAh \cdot g^{-1}$)	References
PVDF-HFP CPE	112 (0.1 C)	85% (0.5 C, 500 cycles)	76 (5 C)	This work
PVDF-HFP CPE	108.6 (0.1 C)	98% (0.1 C, 100 cycles)	89.8 (0.5 C)	[1]
PVDF-HFP CPE	110 (200 $mA \cdot g^{-1}$)	94.1% (200 $mA \cdot g^{-1}$, 400 cycles)	92 (1000 $mA \cdot g^{-1}$)	[2]
PVDF-HFP CPE	95 (0.2 C)	90% (0.1 C, 100 cycles)	52 (5 C)	[3]
PEO CPE	109 (0.1 C)	97.1% (0.5 C, 100 cycles)	66 (1 C)	[4]
PEO CPE	102 (20 $mA \cdot g^{-1}$)	91% (100 $mA \cdot g^{-1}$, 1000 cycles)	70 (1000 $mA \cdot g^{-1}$)	[5]
PE-PEO SPE	116 (1 C)	83% (0.2 C, 250 cycles)	90 (2 C)	[6]
PAN CPE	100.48 (0.1 C)	92.02% (0.2 C, 200 cycles)	82.58 (1 C)	[7]
PVDF-PMMA SPE	97.1 (0.3 C)	97% (1C 200 cycles)	68.7 (30 C)	[8]

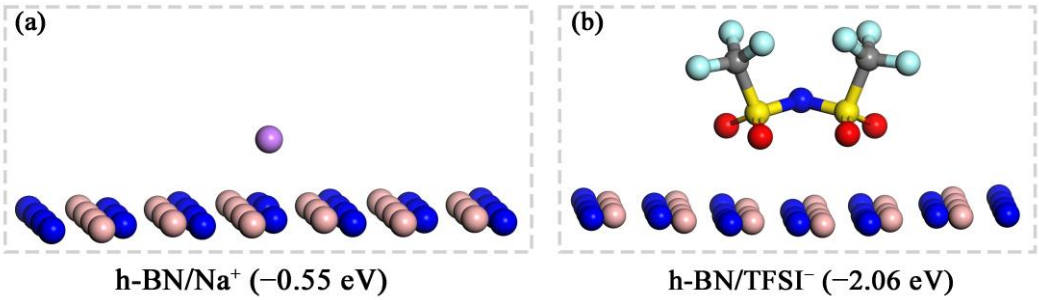

Fig. S1. The adsorption energy of dissociated (a) Na^+ and (b) $TFSI^-$ on h-BN.

In order to investigate the mechanism of h-BN in PVDF-HFP/NaTFSI/BN CPEs, the interactions of h-BN with Na^+ and $TFSI^-$ were investigated by using density functional theory (DFT) calculations. As shown in Fig. S1, the adsorption energies of dissociated Na^+ and $TFSI^-$ on h-BN are −0.55 eV and −2.06 eV, respectively. This result indicates that the interaction between h-BN and $TFSI^-$ is much stronger compared with Na^+. Also, the weak interaction between Na^+ and h-BN may facilitate the rapid migration of dissociated Na^+.

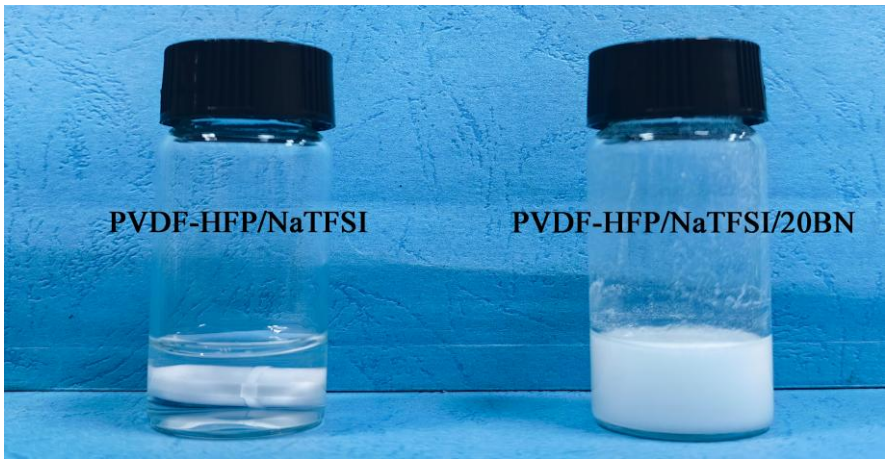

Fig. S2. Digital images of PVDF-HFP/NaTFSI and PVDF-HFP/NaTFSI/20BN solutions.

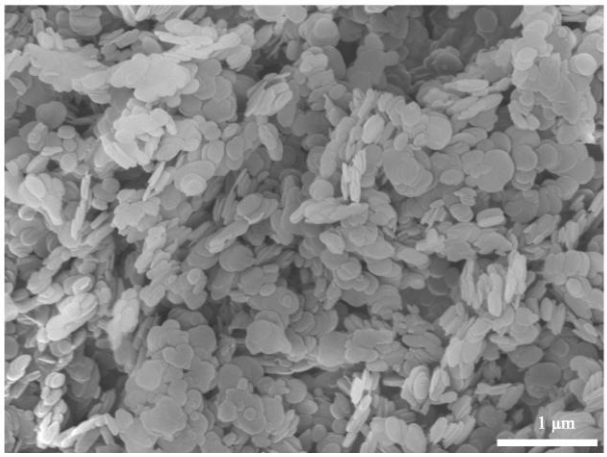

Fig. S3. SEM image of h-BN.

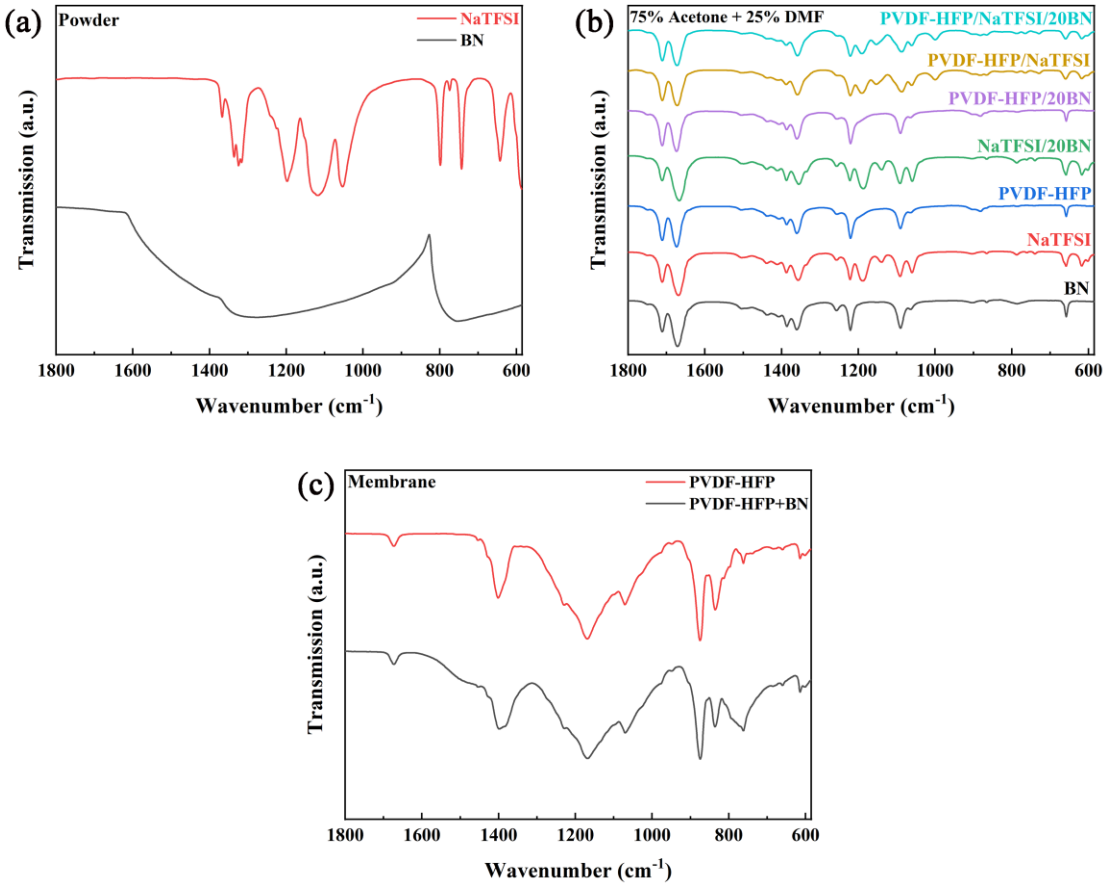

Fig. S4. FTIR spectra of (a) powders, (b) solvents, and (c) membrane of the samples.

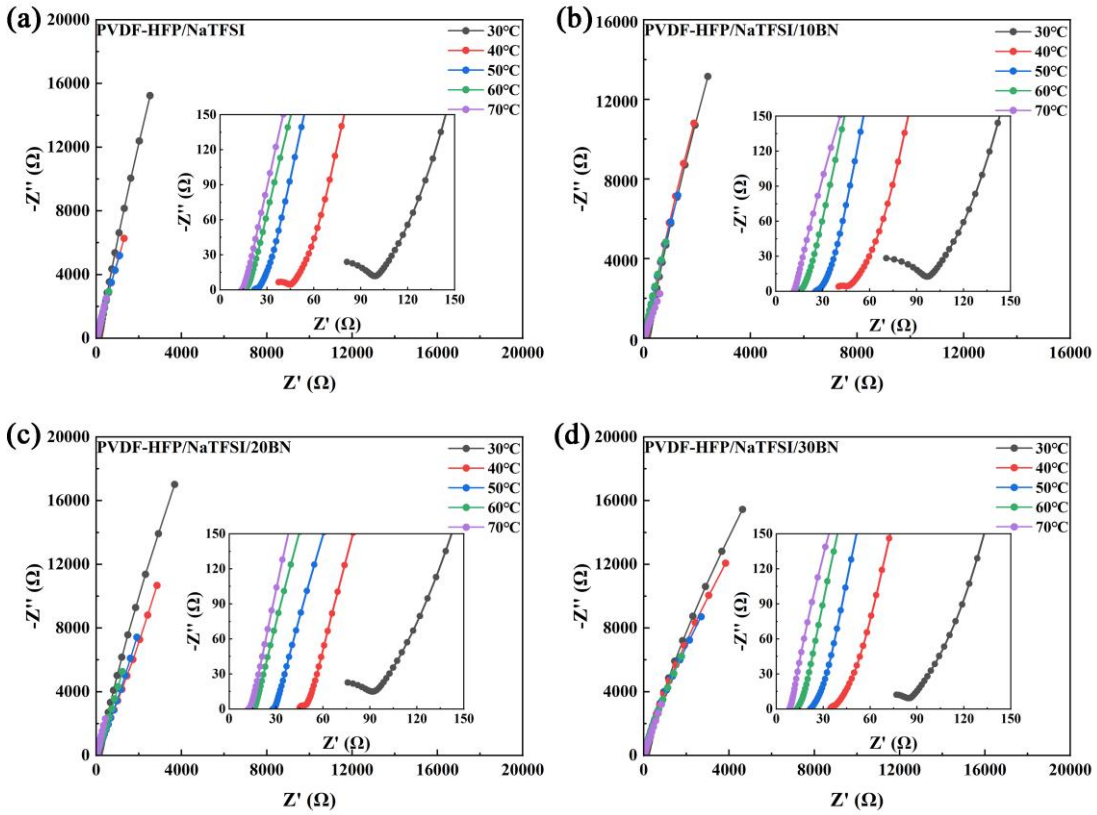

Fig. S5. EIS curves of (a-d) various SSEs from 30 to 70 ℃.

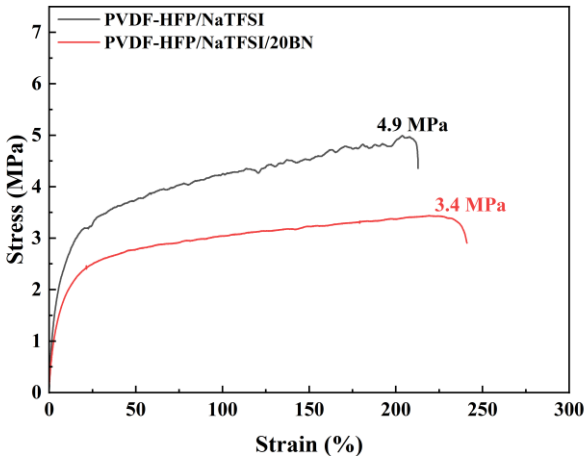

Fig. S6. Tensile test for PVDF-HFP/NaTFSI SPE and PVDF-HFP/NaTFSI/20BN CPE.

Fig. S7. Digital image of PVDF-HFP/NaTFSI/20BN CPE in stretched condition.

From the tensile tests (Fig. S6 and S7), PVDF-HFP/NaTFSI/20BN CPE shows better ductility than PVDF-HFP/NaTFSI SPE, which ensures good interfacial contact with rigid electrodes during cycling.

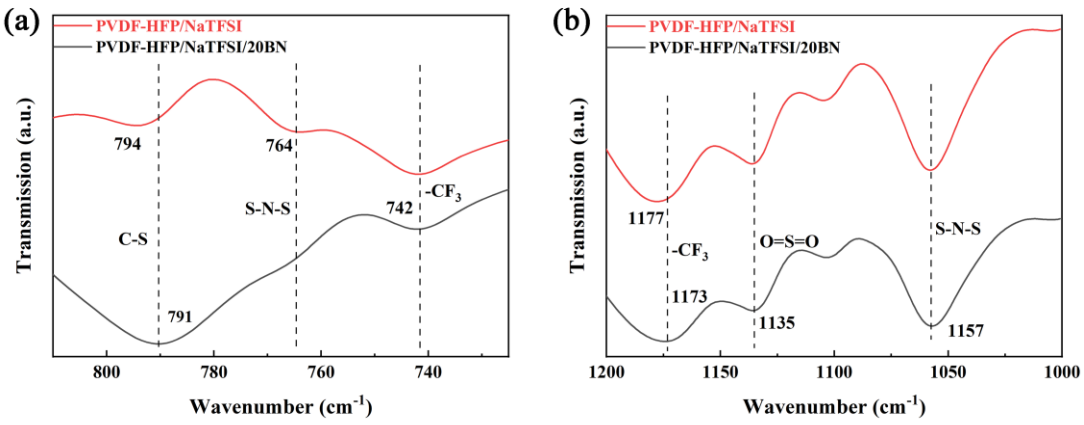

Fig. S8. FTIR spectra of PVDF-HFP/NaTFSI SPE and PVDF-HFP/NaTFSI/20BN CPE at (a) 725−810 cm^{-1} and (b) 1000−1200 cm^{-1}, respectively.

The C−S characteristic peak at 791 cm^{-1} and the $-CF_3$ characteristic peak at 1173 cm^{-1} of the PVDF-HFP/NaTFSI/20BN CPE significantly shift (Fig. S8), and these results emphasize the interaction between h-BN and $TFSI^-$.

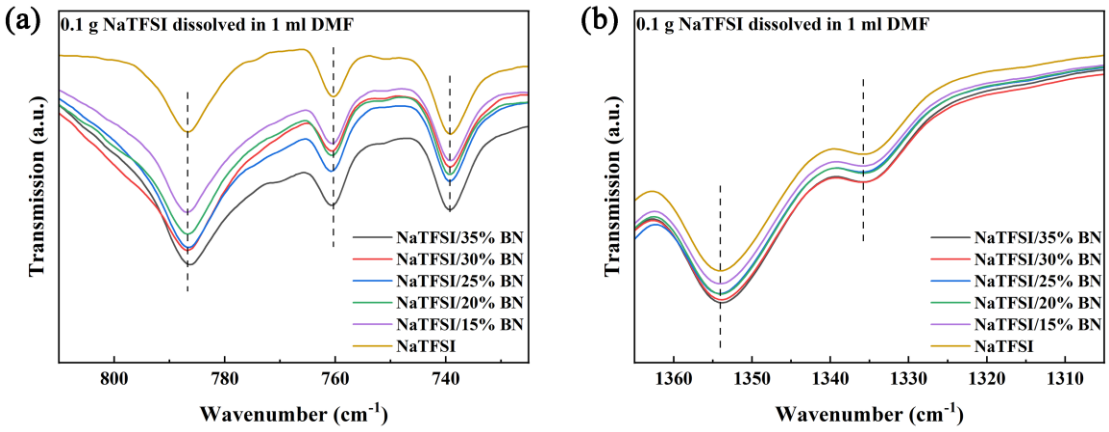

Fig. S9. FTIR spectra of mixed solutions of NaTFSI and BN with different content dissolved in 1 mL DMF at (a) 725−810 cm^{-1} and (b) 1305−1365 cm^{-1}, respectively.

In order to study the interaction between h-BN and $TFSI^-$ more intuitively, h-BN with different contents was sequentially added to 1 mL DMF dissolved with 0.1 g NaTFSI, and these mixtures were subjected to FTIR tests under the same experimental parameters. As shown in Fig. S9, with the increase of h-BN content, the intensity and position of the characteristic peaks change significantly, which implies the interaction between h-BN and $TFSI^-$.

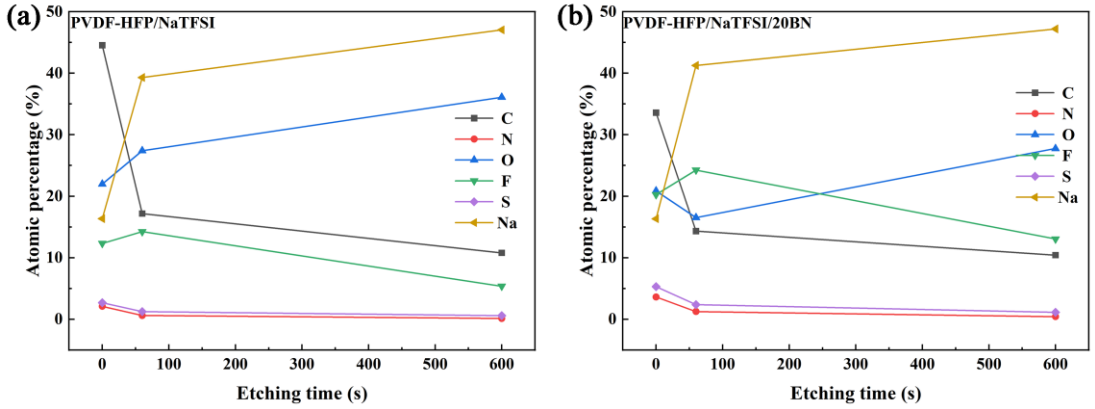

Fig. S10. Corresponding to the atomic concentration of (a) PVDF-HFP/NaTFSI SPE and (b) PVDF-HFP/NaTFSI/20BN CPE at different sputtering.

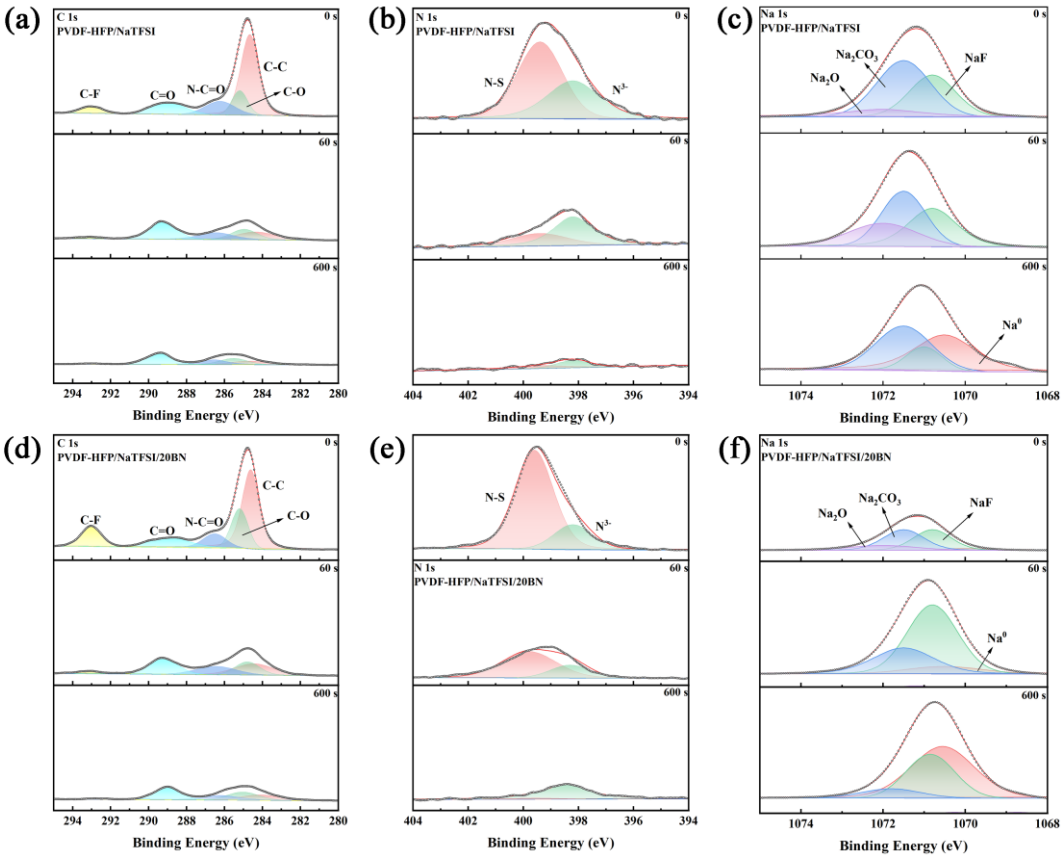

Fig. S11. XPS spectra for C 1s, N 1s, and Na 1s of cycled SMA of (a-c) PVDF-HFP/NaTFSI SPE and (d-f) PVDF-HFP/NaTFSI/20BN CPE.

From the Na 1s spectra in Fig. S11c, it can be seen that a large amount of Na_2CO_3 is generated on the surface of the SMA in contact with the PVDF-HFP/NaTFSI SPE, and Na_2CO_3 is still the most abundant even at 60 s of etching, whereas the Na metal is not observed until after 600 s of etching. This indicates that the SEI formed between the PVDF-HFP/NaTFSI SPE and the SMA has a complex composition and NaF does not play a major role, resulting in the formation of an inhomogeneous and thick SEI, which is unfavorable for long-term cycling of the SSBs. In contrast, the SEI formed by PVDF-HFP/NaTFSI/20BN CPE with SMA has a more homogeneous composition and the sodium metal appears after 60 s of etching, which is also indicative of a thinner SEI (Fig. S11f).

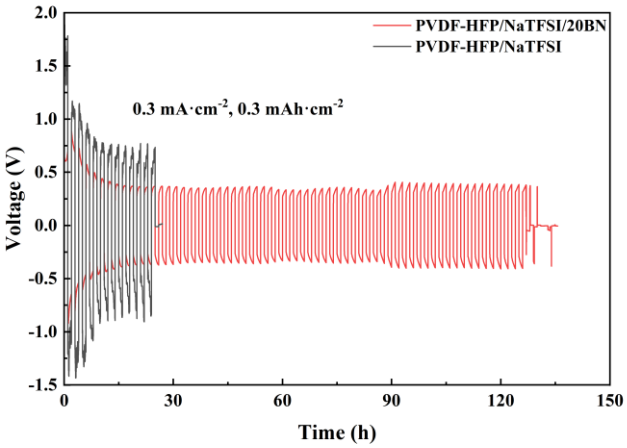

Fig. S12. Galvanostatic cycling curves of Na|0BN|Na and Na|20BN|Na cells under the current density of 0.3 mA·cm^{-2} at 30 °C.

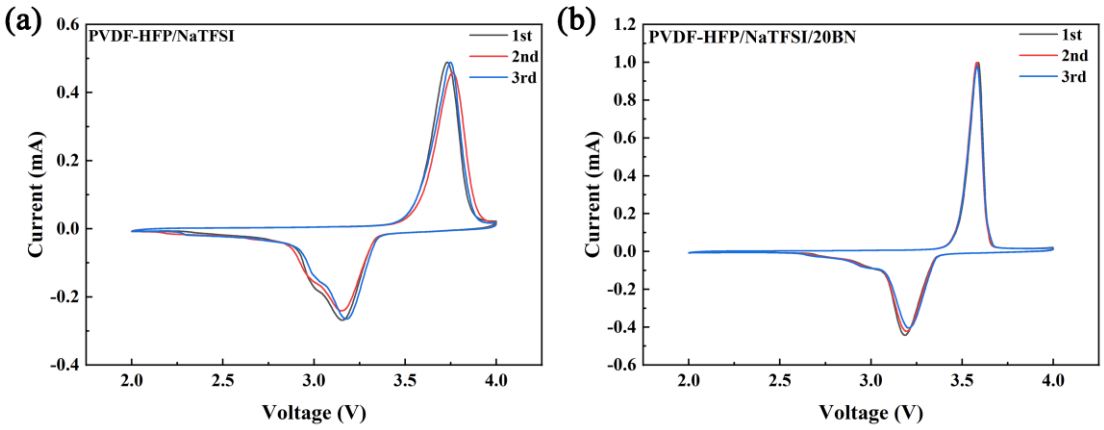

Fig. S13. CV curves of (a) NVP|0BN|Na and (b) NVP|20BN|Na cells.

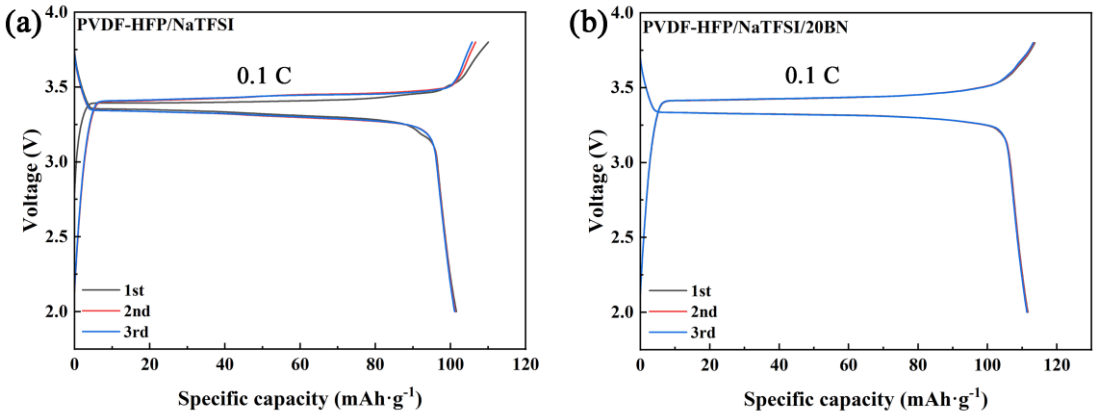

Fig. S14. Charge-discharge voltage profiles of (a) NVP|0BN|Na and (b) NVP|20BN|Na cells at the first three cycles.

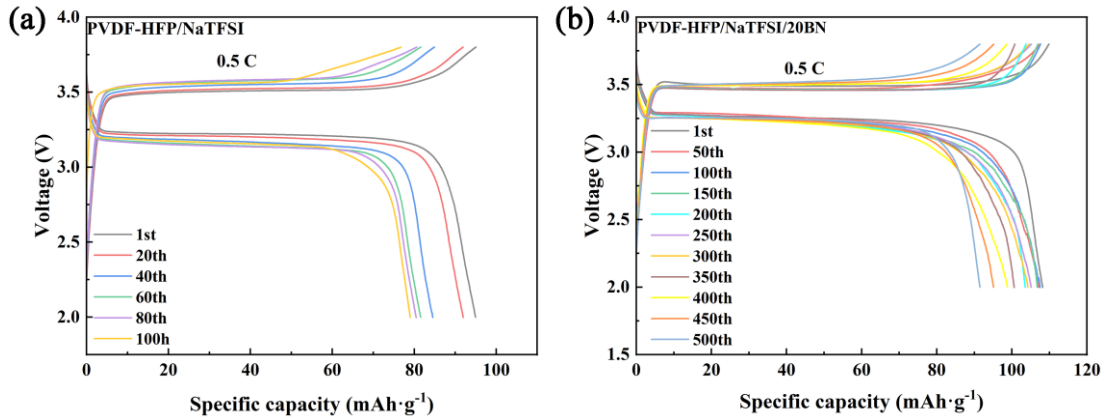

Fig. S15. Charge-discharge voltage profiles of (a) NVP|0BN|Na and (b) NVP|20BN|Na cells at varied cycles.

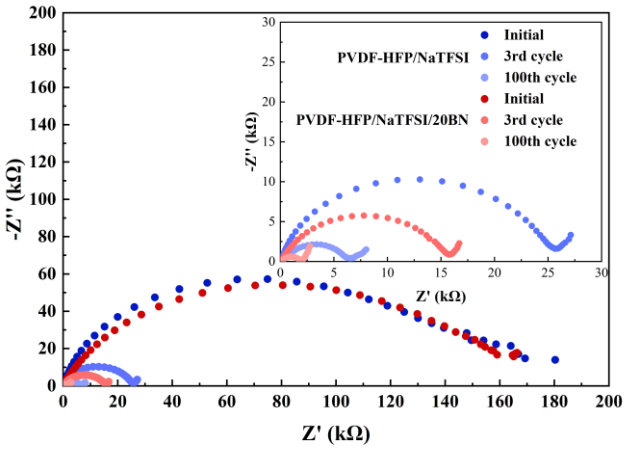

Fig. S16. EIS of NVP|0BN|Na and NVP|20BN|Na cells at different cycles at 30 °C.

The interfacial impedances of the NVP|0BN|Na and NVP|20BN|Na cells were measured. As shown in Fig. S16, the NVP|20BN|Na cell exhibits lower impedance values after the same number of cycles, which is attributed to the lower polarization and better interfacial stability of PVDF-HFP/NaTFSI/20BN CPE.

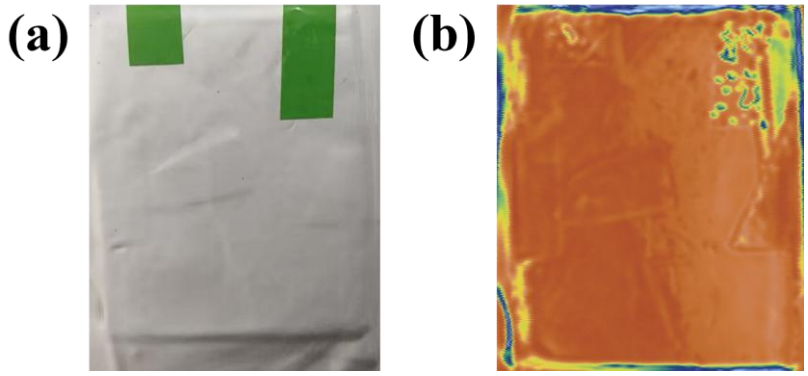

Fig. S17. (a) Digital image and (b) ultrasonic transmission image of NVP|20BN|Na pouch cell.

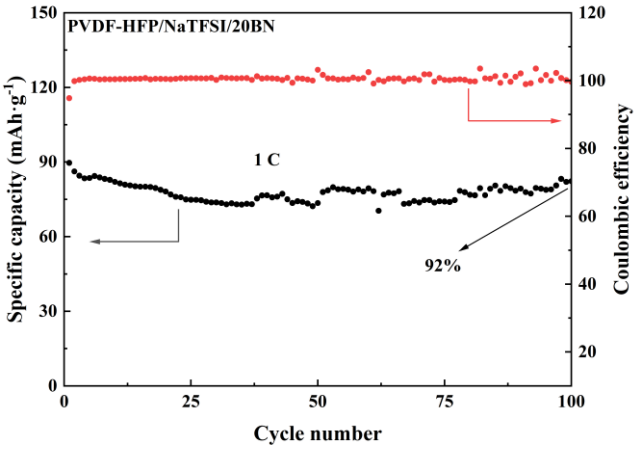

Fig. S18. Long-term cycling performance of NVP|20BN|Na pouch cell.

Fig. S17 shows the digital image and ultrasound transmission image of the NVP|20BN|Na pouch cell. The homogeneous ultrasound image can demonstrate the good interfacial contact between the PVDF-HFP/NaTFSI/20BN CPE and the electrode, which is attributed to the excellent ductility of the PVDF-HFP/NaTFSI/20BN CPE. The NVP|20BN|Na pouch cell exhibits excellent long-term cycling performance, with 92% capacity retention for 100 cycles at 1 C (Fig. S18), which demonstrates the potential of PVDF-HFP/NaTFSI/20BN CPE for practical applications.

References

1. J.-L. Gao, X.-L. Zhao, X.-Q. Ni, Y.-H. Mo, Y.-B. Tong, D.-Q. Cao, H.-B. Luo, Q. Qiao and X.-M. Ren, *ACS Appl. Energy Mater.*, 2024, **7**, 10196-10202.
2. W. Tian, Z. Li, L. Miao, Z. Sun, Q. Wang and L. Jiao, *Adv. Mater.*, 2024, **36**, 2308586.
3. W. Ling, N. Fu, J. Yue, X.-X. Zeng, Q. Ma, Q. Deng, Y. Xiao, L.-J. Wan, Y.-G. Guo and X.-W. Wu, *Adv. Energy Mater.*, 2020, **10**, 1903966.
4. L. Zhao, M. Hou, K. Ren, D. Yang, F. Li, X. Yang, Y. Zhou, D. Zhang, S. Liu, Y. Lei and F. Liang, *Small Methods*, 2024, **8**, 2301579.
5. F. Ling, J. Diao, Y. Yao, R. Bai, Z. Li, M. Ma, Z. Li, H. Huang, S. Zhu, X. Rui, Y. Shao, G. Henkelman and Y. Yu, *Adv. Funct. Mater.*, 2025, **n/a**, 2419970.
6. J. Zhang, Y. Su, Y. Qiu, X. Zhang, F. Xu and H. Wang, *ACS Appl. Mater. Interfaces*, 2024, **16**, 30128-30136.
7. Y. Cui, P. Zhang, Y. Tian, C. Wang, S. Wang, Y. Zhang, X. Shi, Y. Ma, D. Song, H. Zhang, K. Liu, N. Zhang and L. Zhang, *Chem. Eng. J.*, 2024, **498**, 155375.
8. X. Li, Z. Zheng, W. Guo, G. Fu and Y. Zhu, *Macromol. Rapid Commun.*, 2025, **46**, 2400689.